Journal of Biomechanics 195 (2026) 113126

Contents lists available at ScienceDirect

Journal of Biomechanics

journal homepage: www.elsevier.com/locate/jbiomech

Strongly coupled fluid-structure interaction analysis of TEVAR with double-branched endograft for non-A non-B aortic dissection: a patient-specific case study

Binghuan Li [a], Yu Zhu [a,b], Kaihong Wang [a], Sandro Lepidi [c], Mario D'Oria [c], Xiao Yun Xu [a,*]

[a] Department of Chemical Engineering, Imperial College London, UK
[b] National Heart and Lung Institute, Imperial College London, UK
[c] Division of Vascular and Endovascular Surgery, Department of Medical Surgical and Health Sciences, University of Trieste, Italy

ARTICLE INFO

Keywords:
TEVAR
Fluid-Structure Interaction
Branched stent-graft
Haemodynamics

ABSTRACT

Thoracic endovascular aortic repair (TEVAR) with branched devices has shown its promise in the treatment of complex thoracic aortic pathologies such as chronic aortic dissection involving the aortic arch. Understanding the short-term and long-term biomechanical changes remains essential for the prediction of possible adverse events and optimising post-operative patient care. This study presents a patient-specific haemodynamic and biomechanical evaluation of a branched TEVAR device by performing two-way fluid-structure interaction (FSI) simulation. The geometric model was reconstructed from the computed tomography angiography scan, and the additional branch configurations were constructed based on the measured orientation and device-specific dimensions. The native aortic wall was modelled as an anisotropic hyperelastic material, and strongly coupled FSI simulations were conducted with three-dimensional velocity profiles at the inlet and Windkessel boundary conditions at the outlets. Our FSI simulation results captured physiologically realistic flow dynamics, wall shear stress distributions, and displacement forces (up to 14.95 N), revealing both favourable outcomes and regions of potential thrombotic risk. In particular, low wall shear stress (< 0.4 Pa) and high relative residence time (> 15 Pa^{-1}) were observed in the left common carotid artery branch, correlating with thrombus formation observed in a follow-up scan, whereas such regions were underestimated by the rigid-wall computational fluid dynamics simulation. Wall stress analysis revealed peak von Mises stresses exceeding 600 kPa at the proximal and distal landing zones of the stent-graft due to compliance mismatch. These findings underscore the potential value of incorporating wall compliance into the computational workflow for post-TEVAR evaluation, offering more accurate prediction of adverse events and informing patient-specific long-term monitoring strategies.

1. Introduction

Thoracic endovascular aortic repair (TEVAR) has increasingly been accepted as an effective approach for managing most thoracic aortic diseases (D'oria et al., 2025), including selected cases involving the aortic arch, with favourable short-term and mid-term technical and clinical outcomes (Iglesias Iglesias et al., 2023, Negmadjanov et al., 2021). Continued advancements of the stent-grafts (SG) technologies have enabled the incorporation of patient-specific anatomical variations, such as the aortic curvature, lengths, and angulation, enhancing the device conformability and enabling the proximal deployment in Ishimaru's zones 0 and 1 which have been traditionally considered challenging due to the complex anatomical features (Ferrer et al., 2024). One such product is the Relay® Branch Thoracic Stent-Graft System (Terumo Aortic, Sunrise, FL, USA) which incorporates two or three inner branches mounted on the main SG body. This design facilitates smooth alignment with the supra-aortic vessels, which is important for maintaining normal perfusion to the aortic arch branches. Using the double-branched configuration, targeted revascularization of the innominate artery (IA) and left common carotid artery (LCCA) can be achieved, while perfusion through the left subclavian artery (LSCA) is usually maintained via a LSCA-LCCA bypass in conjunction with a percutaneous occlusion of the LSCA root (Ferrer et al., 2019).

Existing computational studies of branched endograft systems have

* Corresponding author at: Department of Chemical Engineering, South Kensington Campus, Imperial College London, London SW7 2AZ, United Kingdom.
E-mail addresses: binghuan.li19@imperial.ac.uk (B. Li), yu.zhu14@imperial.ac.uk (Y. Zhu), k.wang21@imperial.ac.uk (K. Wang), slepidi@units.it (S. Lepidi), MARIO.DORIA@units.it (M. D'Oria), yun.xu@imperial.ac.uk (X.Y. Xu).

https://doi.org/10.1016/j.jbiomech.2025.113126
Accepted 11 December 2025
Available online 11 December 2025

mainly focused on the analysis of haemodynamic alterations in the aorta following the SG deployment (Zhu et al., 2019, Sengupta et al., 2022a, Van Bakel et al., 2018, Zhang et al., 2024, Chiu et al., 2018, Qiao et al., 2020, Ruggeri et al., 2025, Ye et al., 2025). Results from rigid-wall computational fluid dynamics (CFD) simulations have demonstrated that TEVAR can effectively restore more organised and physiologically favourable blood flow, reducing the chaotic and disturbed flow patterns typically observed in the diseased aortas. Common observations – including improved flow patency in the true lumen of dissected aortas and supra-aortic branches, enhancement of helical flow structures, elimination of the local recirculation zones, moderate increase in wall shear stress (WSS) and reduction in relative residence time (RRT) – indicate a favourable haemodynamic environment owing to the intervention.

However, the resulting changes in flow dynamics following SG implantation can be complex and often yield both beneficial and adverse effects. One of the key concerns is the risk of intraluminal thrombus formation, which may arise from the activation of platelets due to elevated WSS. Conversely, regions with low WSS – typically associated with local flow stagnation and prolonged residence time – can promote platelet adhesion and thrombosis (Zambrano et al., 2016). In addition to thrombotic risks, flow-induced displacement forces acting on the SG and aortic wall, arising from the pressure and WSS, are critical in assessing the overall device performance, such as the risk of device migration or endoleaks (Kandail et al., 2014, Sengupta et al., 2022b). Last but not least, the magnitude and transmission of these forces are strongly influenced by the mechanical interaction between the SG and the surrounding tissue (Da Silva et al., 2023a, Van Bakel et al., 2019), as seen for example in distal SG-induced new entry (dSINE) (Menichini et al., 2018, D'oria et al., 2024, Burdess et al., 2022). As such, rigid-wall CFD models, which neglect vessel compliance, may compromise the fidelity of physiologically accurate and, as a result, clinically relevant predictions.

Current studies of branched-TEVAR have not yet simultaneously assessed the combined haemodynamic and structural responses of inner branch modules in a patient-specific setting, leaving a critical gap in predicting post-operative risks. To address this, the present work aims to perform a strongly coupled FSI analysis of a patient-specific branched thoracic endograft in a single post-operative scenario, focusing on the haemodynamic environment and SG loading conditions to support early identification of possible adverse effects, including thrombosis and device failure. Furthermore, comparisons between the conventional CFD and FSI simulation results were conducted to quantify the impact of aortic compliance on the haemodynamic outcomes.

2. Materials and methods

2.1. Patient data acquisition, device specification, and CTA processing

The research was authorised by the ethical committee of the involved institutions. The patient had previously given informed consent for use of anonymized data and images for retrospective research. Thin-slice, triphasic, ECG-gated computed tomography angiography (CTA) scan was acquired from a 66-year-old male patient with chronic non-A non-B aortic dissection 6 months after technically successful TEVAR using a custom-made Relay® Branch Thoracic Stent-Graft System. An additional 24-month follow-up CTA scan confirmed the presence of a thrombus near the distal end of the LCCA inner branch while under antiplatelet therapy. All scans were performed on a GE Revolution EVO scanner (GE Healthcare, Chicago, IL, USA). The TEVAR device consisted of a 270-mm main SG module, and two antegrade inner branches latched to the main body. The proximal and distal landing zones of the main SG measured 46 mm and 30 mm in diameter, with a proximal SG oversizing ratio of 1.21. Both inner branches have an inner tunnel diameter of 13 mm, while the outer tunnel diameter is 18 mm for IA and 8 mm for LCCA. The SG coverage of LSCA necessitated its occlusion and a bypass procedure to reroute blood from the LCCA.

The multi-slice CTA images were processed using Materialise Mimics 24.0 (Materialise, Leuven, Belgium). Employing the semi-automated thresholding and region-growing method, the images were initially segmented along the transverse plane, and the resulting image masks for the isolated aorta were further refined manually prior to the reconstruction of the 3D geometric model. However, due to the presence of imaging artefacts and the metallic nature of the stent struts, the fine details of the inner branches were not sufficiently resolved in the CTA data to allow for accurate branch reconstruction. As such, a second step was implemented to reconstruct the branch configurations of the TEVAR device. As illustrated by Fig. 1, the centrelines of the two inner branches were computed from the segmented masks and, together with the dimensional specifications, were used to guide the reconstruction of the branch configurations in SolidWorks 2023 (Dassault Systemes, Velizy-Villacoublay, France).

2.2. Mesh generation and mesh sensitivity analysis

The success of an FSI simulation relies on the accurate transfer of physical data across the fluid-structure interface; therefore, ensuring the topological consistency between the fluid and structure domains is critical to achieve stable coupling. Given the added complexity of the geometric model introduced by the presence of additional inner branch modules, the solid and fluid meshes were generated simultaneously. The structural domain was constructed by uniformly offsetting the CTA segmentation outward by 1.5 mm (Zhu et al., 2025b). For the branch components, a similar method was applied, but with a wall thickness of 0.4 mm (Jorgensen and Paaske, 1998). The aortic wall and inner branch modules were subsequently assembled by matching and joining the intersected surfaces. Following the surface assembly, a solid mesh was created in ANSYS ICEM CFD 23R2 (ANSYS Inc., Canonsburg, PA, US) with tetrahedral elements, whereas the volume enclosed by the aortic wall and inner branches was identified as the fluid domain and meshed separately in a similar manner. The resulting meshes are shown in Fig. 2 (a).

To achieve a balance between simulation time and accuracy, three different mesh configurations were tested with varying element sizes and refinement levels. For the fluid domain, spatially averaged pressure and WSS at peak systole were compared, while spatially averaged deformation and von Mises stress were used to assess the structural domain. The selected mesh, consisting of approximately 3.1 million fluid elements and 1.2 million solid elements, showed less than 4% differences in all evaluated parameters compared to the finest mesh. Further details about the grid independence analysis can be found in Supplementary Material S1.

2.3. Governing equations and boundary conditions

2.3.1. Fluid domain

In this study, the blood was modelled as an incompressible, Newtonian fluid governed by the continuity and the Navier-Stokes equations, namely

$$\nabla\cdot\mathbf{v} = 0, \tag{1}$$

$$\rho_f\left(\frac{\partial\mathbf{v}}{\partial t} + (\mathbf{v}-\mathbf{v}_f)\cdot\nabla\mathbf{v}\right) = -\nabla p + \nabla\cdot\boldsymbol{\tau}_f + \mathbf{f}, \tag{2}$$

where $\mathbf{v} = [v_x, v_y, v_z]$ is the fluid velocity vector, p is the fluid pressure, $\rho_f = 1060\ \mathrm{kg/m^3}$ is the fluid density, $\mathbf{v}_f$ is the moving boundary velocity on the fluid-structure interface. Finally, $\boldsymbol{\tau}_f = 2\mu\mathbf{e}$ is the fluid shear stress raising from the fluid motion, with $\mathbf{e}$ being the strain rate tensor and μ being the dynamic viscosity at 0.0035 Pa·s.

Due to the lack of 4D flow magnetic resonance imaging (MRI) data, a personalised synthetic 4D velocity profile was employed as the inlet

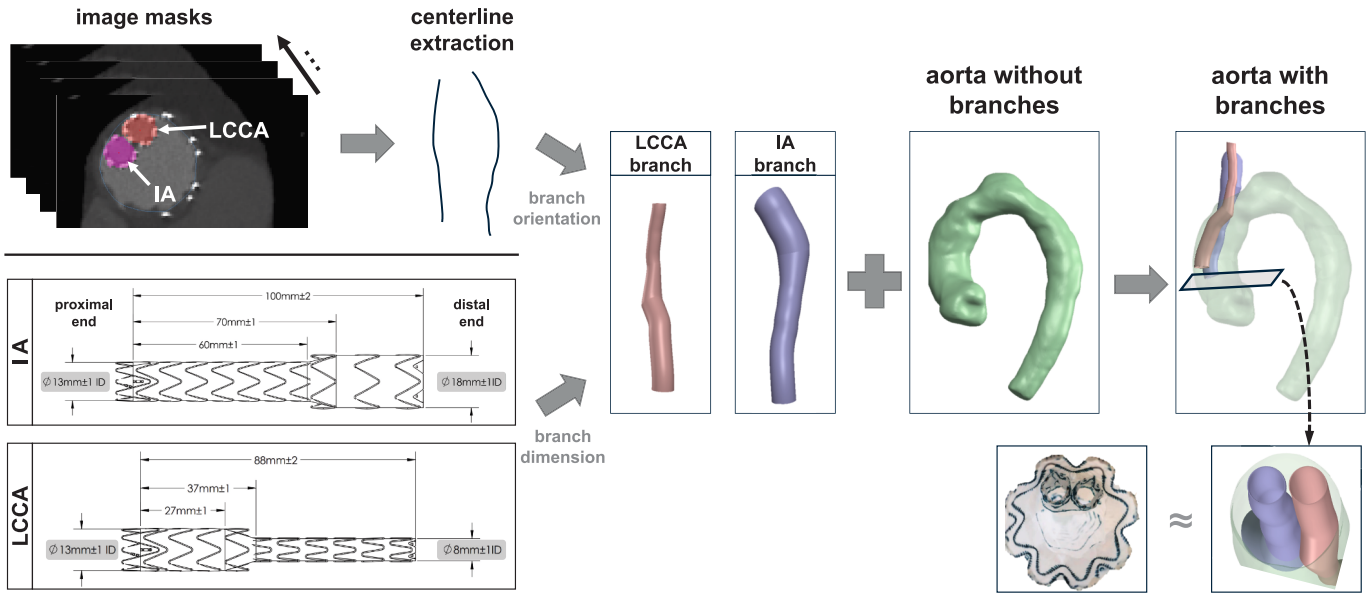

Fig. 1. Summary of key stages for the reconstruction of the branch configurations in post-TEVAR geometries.

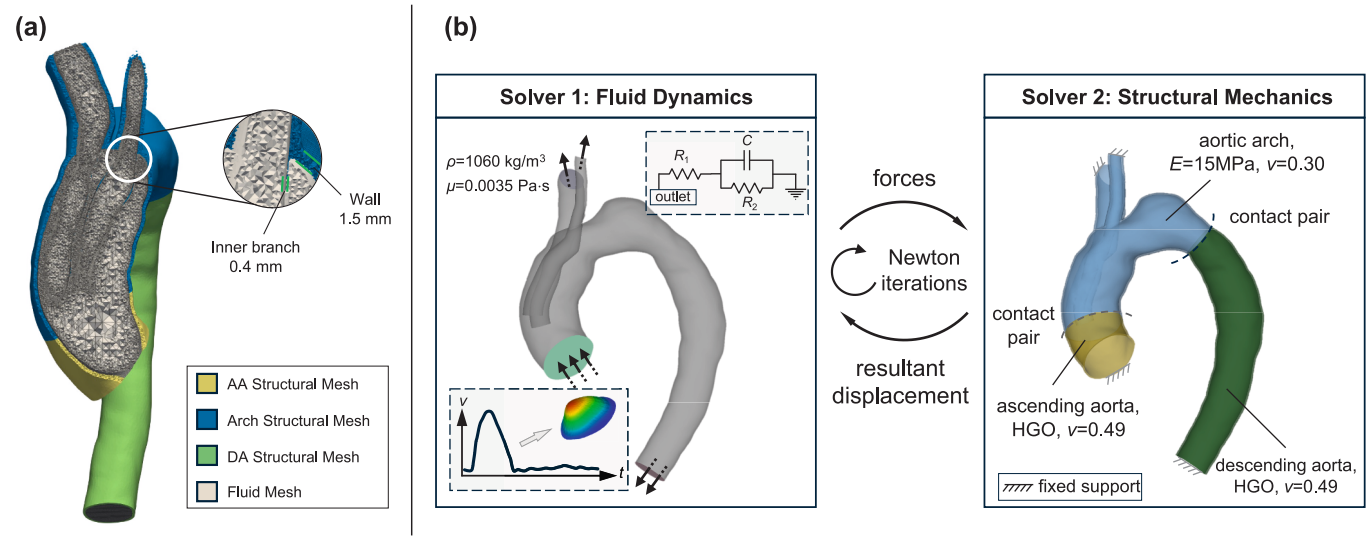

Fig. 2. **(a)** Details of the mesh at the inner branch region, showing the fluid mesh (grey) and the structural mesh (yellow: AA, blue: arch, green: DA). For the structural mesh, the vessel wall thickness is 1.5 mm and the inner branch wall thickness is 0.4 mm. **(b)** Schematic of the FSI simulation setup. (For interpretation of the references to colour in this figure legend, the reader is referred to the web version of this article.)

boundary condition. Following the method proposed by Saitta et al. (Saitta et al., 2023) and further extended by Wang et al. (Wang et al., 2025) for dissected patients, a spatial- and temporal-varying profile synthesized from the statistical shape regression and principal component analysis was selected and calibrated using the patient-specific stroke volume (60 ml) and heart rate (61 bpm) obtained from cardiac echocardiogram measurements. The calibrated inlet velocity profile exhibited a flow skewness, with a flow asymmetry index of 7.72% and a flow dispersion index of 46.0% at peak systole (Fig. 3a), compared with 0% and 15%, respectively, for an idealized parabolic profile.

The pressure-type, 3-element Windkessel model was prescribed at each model outlet, with parameter values calculated from the flow split ratio estimated using measured cross-sectional areas (Table 1). To account for the LSCA-LCCA bypass in the post-TEVAR configuration, the distal resistance at the LCCA outlet was adjusted. This was done by combining the pre-TEVAR distal resistances of the LCCA and LSCA in parallel, ensuring the total LCCA flow matched the post-TEVAR condition (Zhu et al., 2019):

$$R_{\mathrm{LCCA,\ post}} = \frac{1}{\frac{1}{R_{\mathrm{LCCA,\ pre}}} + \frac{1}{R_{\mathrm{LSCA,\ pre}}}}, \tag{3}$$

2.3.2. Structural domain

The dynamical behaviour of the solid is governed by the equation of motion, as

$$\nabla \cdot \boldsymbol{\sigma}_s = \rho_s \ddot{\mathbf{u}}_s, \tag{4}$$

where σ_s is the Cauchy stress tensor, ρ_s is the density of the solid material, and $\ddot{\mathbf{u}}_s$ is the local acceleration, defined as the second-order derivative of the displacement, $\mathbf{u}$.

As shown in Fig. 2, the post-TEVAR aorta was divided into the stented and unstented regions, with a general contact algorithm prescribed to maintain the attachment of each segment. The unstented section covers the ascending aorta and the descending aorta, and it was

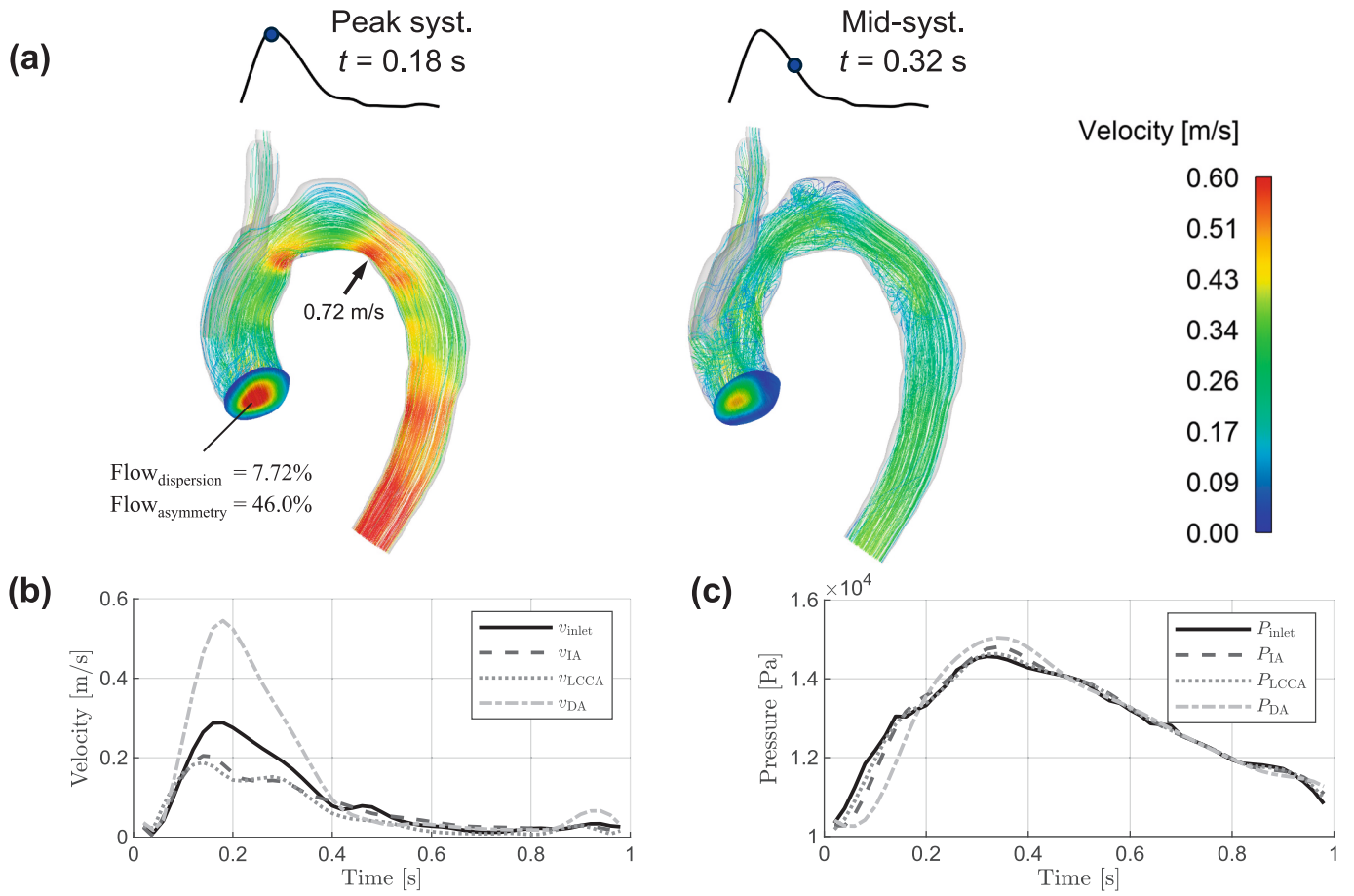

Fig. 3. Flow characteristics. (a) Streamlines and velocity fields at peak systole, mid-systole, and mid-diastole show flow patterns in the aorta. Spatial-averaged (b) velocity and (c) pressure plots at inlet/outlet locations illustrate temporal haemodynamic changes.

Table 1
Summary of Windkessel parameters for model outlets and simulated flow split ratio (rounded to the nearest integer). R_1 and R_2 denote the proximal and distal resistances, respectively, and C denotes the vessel compliance. IA – innominate artery; LCCA – left common carotid artery; DA – descending aorta.

	R_1 [$\times 10^7$ Pa·s·m^{-3}]	R_2 [$\times 10^8$ Pa·s·m^{-3}]	C [$\times 10^{-9}$ m^3·Pa^{-1}]	Flow Split (%)
IA	2.85	10.7	1.64	15
LCCA	17.9	52.1	0.33	12
DA	0.40	2.70	6.53	73

modelled as an anisotropic hyperelastic material with a density of 1100 kg·m^{-3}, using the Holzapfel-Gasser-Ogden (HGO) constitutive model. The strain-energy density function, Ψ, is defined as:

$$\Psi = \frac{c}{2}(I_1 - 3) + \frac{k_1}{2k_2}\sum_{i=4,6}[e^{(k_2(I_i-1)^2)}-1], \quad (5)$$

where c, k_1, k_2 are material parameters representing the isotropic material stiffness, anisotropic fibre stiffness, and fibre stiffening factor, respectively; I_1 is the first invariant of the Cauchy-Green deformation tensor, and I_4 and I_6 are the pseudo-invariants. In this study, c, k_1, k_2 were set to 109 kPa, 164.37 kPa and 4.1787 respectively, based on biaxial tensile testing performed on dissected aortic tissue samples (Subramaniam et al., 2021). The fibre orientations were described using local material axes, with orthogonal vectors obtained by solving Dirichlet-Laplace problems in the inlet–outlet and endothelium-epicardium directions (Schussnig et al., 2022). For the stented region, the aortic wall and SG were assumed to be tied together, with no gap, reflecting a complete SG integration six months post-TEVAR. Therefore, this composite region was modelled using an effective linear elastic modulus of 15 MPa, a density of 2140 kg·m^{-3}, and a Poisson's ratio of 0.3 (Sengupta et al., 2023, De Bock et al., 2013).

To avoid any rigid body motion, an encastre boundary condition was applied to fix the inlet and outlet ends of the structural domain, as well as the ends of the inner branch modules. Empirical Rayleigh damping was prescribed with $\alpha = 50$ and $\beta = 0.1$ to provide realistic dynamic behaviour of the aortic wall for the support by its surrounding tissue (Zhu et al., 2022). Finally, the assembled model was pre-stressed using an iterative scheme, in which a diastolic pressure of 80 mmHg was applied to the inner aortic wall. At this stage, a uniform pressure load was assumed across the stented and unstented regions. The resulting stress tensor was then transferred as the initial stress state for the subsequent simulation. This process was repeated until the maximum deformation was reduced to less than 0.5 mm (Zhu et al., 2025a, Zhu et al., 2025b).

2.4. Fluid-Structure domain coupling

For the FSI simulation (Fig. 2(b)), the CFD solver ANSYS Fluent and implicit finite element solver ANSYS Transient Structural were coupled using System Coupling 24R1 (ANSYS Inc., Canonsburg, PA, US). A fixed time step of 0.001 s was employed for both solvers. At each time step, data exchange was performed iteratively using a quasi-Newton scheme, with a maximum number of 5 data exchange iterations allowed, until the convergence was achieved in both the fluid and structural solvers. A 1×10^{-2} RMS convergence target was applied to enforce the continuity of displacement, velocity, and force at the fluid-structure interface. An

under-relaxation factor of 0.75 was applied to the transfer of fluid loads to the structure domain, while no relaxation was applied to the return transfer of structural deformation to the fluid domain.

2.5. Post Processing of simulation results

Time-averaged wall shear stress (TAWSS) is a scalar variable computed by averaging the magnitude of instantaneous wall shear

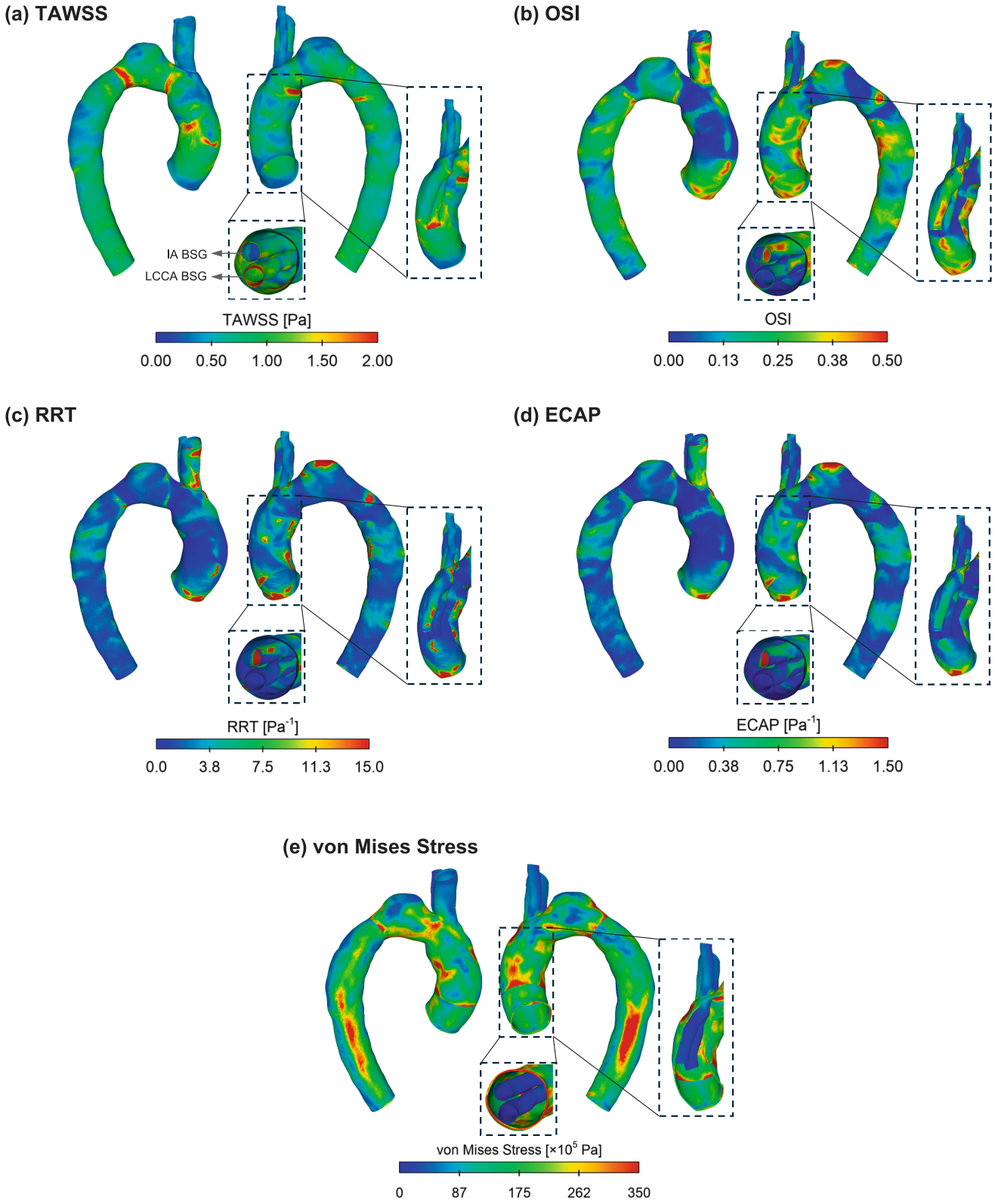

Fig. 4. Spatial distribution of haemodynamic and biomechanical parameters in the post-TEVAR aorta. (a) Time-averaged wall shear stress (TAWSS); (b) Oscillatory shear index (OSI); (c) Relative residence time (RRT); (d) Endothelial cell activation potential (ECAP); (e) von Mises stress.

stress, τ_w, over the entire cardiac cycle, T:

$$\mathrm{TAWSS} = \frac{1}{T}\int_0^T |\boldsymbol{\tau}_w|\,\mathrm{d}t. \tag{6}$$

Oscillatory shear index (OSI) is a dimensionless quantity that ranges between 0 and 0.5, measuring the change in directionality of WSS relative to the flow:

$$\mathrm{OSI} = \frac{1}{2}\left(1 - \frac{\left|\int_0^T \boldsymbol{\tau}_w\,\mathrm{d}t\right|}{\int_0^T |\boldsymbol{\tau}_w|\,\mathrm{d}t}\right). \tag{7}$$

The relative residence time (RRT) is a synthetic parameter which indirectly measures the amount of time blood particles reside at the vessel wall,

$$\mathrm{RRT} = \frac{1}{(1 - 2{*}\mathrm{OSI}){*}\mathrm{TAWSS}}. \tag{8}$$

The endothelial cell activation potential (ECAP) is another synthetic haemodynamic matric which combines TAWSS and OSI to characterise the degree of "thrombogenic susceptibility" of the arterial wall,

$$\mathrm{ECAP} = \frac{\mathrm{OSI}}{\mathrm{TAWSS}}. \tag{9}$$

Finally, the displacement force, **F**, is calculated as the integration of the pressure force and WSS force over the surface S of the domain (Kandail et al., 2014),

$$\mathbf{F} = \int_S p{\cdot}\mathbf{n}\mathrm{d}A + \int_S \boldsymbol{\tau}_w \mathrm{d}A. \tag{10}$$

3. Results

Fig. 3 shows the flow characteristics from the FSI simulation. Instantaneous velocity streamlines were captured at two distinct phases across the cardiac cycle: peak systole and mid-systolic deceleration. At peak systole, the streamlines exhibited a smooth, organised pattern well-aligned with the curvature of the aortic wall. The maximum velocity was observed near the distal landing zone, reaching 0.72 m/s. In contrast, mid-systolic deceleration is characterised by reduced velocity magnitude, accompanied by a moderate local flow recirculation adjacent to the bulge to the distal landing zone. Overall vessel patency is achieved throughout the cardiac cycle, where the IA, LCCA, and DA outlets were splitting 15%, 12%, and 73% of the total flow, maintaining adequate blood perfusion to all distal territories. Pressure values at all boundaries were found within the physiological range, from 10666 Pa (80 mmHg) to approximately 15500 Pa (116 mmHg). These findings support the accuracy and physiological relevance of the simulation setup and applied boundary conditions.

Fig. 4 shows the spatial distribution of TAWSS and wall shear-related haemodynamic matrices derived from the FSI simulation. Regions of TAWSS greater than 2 Pa were predominantly observed near the distal landing zone of the SG, and at the proximal end of the IA inner branch. In contrast, low TAWSS values were localised along the inner wall of the LCCA tunnel and near the posterior bulge of the aortic arch, with a distinct iso-volume of 69.15 cm^3. A similar spatial pattern was captured in the distributions of RRT and ECAP, where RRT values $> 15\ Pa^{-1}$ and ECAP values $> 1.5\ Pa^{-1}$ were concentrated within the LCCA branch and in the bulge region adjacent to the distal landing zone, highlighting the presence of flow recirculation and prolonged particle residence in these areas. Consistent with these predictions, the 24-month post-TEVAR follow-up scan confirmed the presence of thrombus at the distal side of the LCCA branch (Fig. 5(b)), validating the haemodynamic findings.

To assess mechanical forces that could contribute to device fatigue or migration, displacement forces were evaluated. The maximum displacement force on the SG was observed during the mid-diastolic phase, peaking at 14.95 N. Spatial analysis revealed that the highest blood pressure during this phase occurred at the distal end of the descending aorta, reaching 15576 Pa. Furthermore, wall stress – quantified using the von Mises criterion (Fig. 4e) – showed elevated stress (> 350 kPa) predominantly concentrated along the inner curvature of the arch and the descending aorta. Notably, peak stresses exceeding 600 kPa were observed at both the proximal and distal landing zones of the SG.

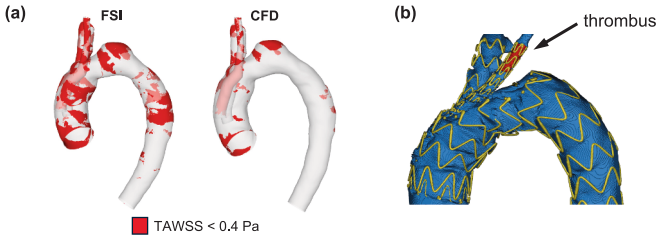

Fig. 5. (a) Iso-volume plots showing regions of low wall shear stress (TAWSS < 0.4 Pa) from FSI and CFD simulations; (b) 24-month post-TEVAR 3D reconstruction highlighting thrombus formation (black arrow) at the distal side of the LCCA branch.

Fig. 6 compares the maximum velocity and pressure at peak systole between the fully coupled FSI and rigid-wall CFD simulations across ten representative locations (P1-P10) along the thoracic aorta. As shown in Fig. 6(a), only subtle differences in the maximum velocity were observed. Generally, FSI predicts slightly lower velocities than CFD, with values ranging from approximately 0.41 m/s to 0.71 m/s. The most notable difference was at P3 and P4, where CFD produced a marginally higher velocity compared to FSI by 0.03 m/s. This difference is likely attributed to the combined influence of local wall compliance captured by FSI and complex flow patterns near the inner branch inlets at P3 and P4. In Fig. 6(b), CFD consistently overestimated the maximum pressure relative to FSI, with differences typically ranging from 500 to over 700 Pa. These results highlighted the dampening effect of wall compliance captured by FSI, which led to reduced peak pressure values. Furthermore, rigid-wall CFD underestimated regions of low WSS (< 0.4 Pa, as shown in Fig. 5(a)), potentially under-predicting the risk of thrombosis in certain areas. Overall, the inclusion of wall compliance through FSI provided a more physiologically realistic representation of haemodynamics, which is critical for accurate prediction of device performance and potential complications in TEVAR procedures.

4. Discussion

This study presents a comprehensive functionality assessment of a customised Relay® Branch Thoracic Stent-Graft System used in the treatment of chronic non-A non-B aortic dissection, using a strongly coupled FSI method. Incorporating physiologically realistic boundary conditions, the results highlight the biomechanical advantages of accounting for wall compliance in TEVAR evaluation and reveal both beneficial and potentially adverse haemodynamic effects.

Implantation of the Relay® Branch Thoracic Stent-Graft led to an organised flow environment across the aortic arch, with streamlined flow patterns and preserved perfusion in all supra-aortic branches, closely matching healthy haemodynamics. Quantitative analysis confirmed physiological velocity magnitudes and pressure distributions, validating the appropriateness of the simulation setup. Although some studies have reported that protruding segment of branch SGs may alter the local haemodynamic environment manifested by the increased degree of flow disturbances (Qiao et al., 2020) and different vortex dynamics (Chiu et al., 2018), such effects were not observed in our case, potentially owing to the lock stent mechanism designed to ensure precise wall-branch alignment and prevent disconnection. However, it was noted that the LCCA branch exhibited a higher peak velocity than the IA branch, likely due to its smaller diameter and the tapering between the inner tunnel and outer branch, and the additional flow needed to supply

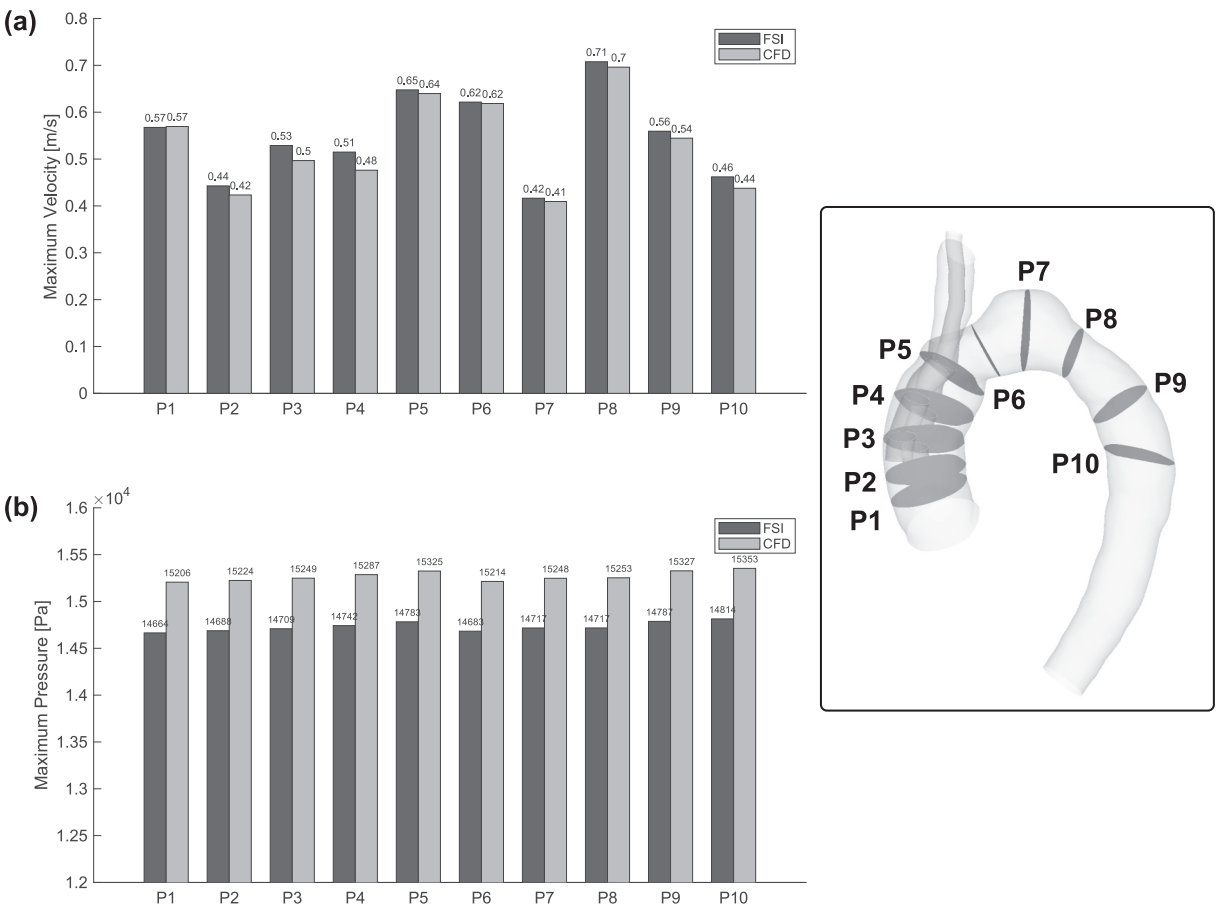

Fig. 6. Comparisons of (a) the maximum velocity and (b) maximum pressure at peak systole between CFD and FSI simulations at 10 representative locations (P1-P10).

the LSCA. This localised acceleration reflects the sensitivity of flow dynamics to geometric changes and reinforces the importance of precise device-patient matching.

Key haemodynamic indices, including TAWSS, RRT, and ECAP, identified disturbed flow regions prone to thrombus. Several studies have linked thrombotic risk to SG design and patient-specific anatomical characteristics. For example, Chiu et al. (Chiu et al., 2018) reported that internal branches introduced oscillatory flow components, potentially increasing thrombogenic risk. van Bakel et al. (Van Bakel et al., 2018) found that antegrade branch configurations outperformed retrograde ones in preserving cervical artery perfusion and reducing shear rate. Zhu et al. (Zhu et al., 2019) showed that, despite adequate perfusion, inner tunnels in the endograft disrupted flow symmetry and elevated WSS in the ascending aorta, raising concerns over long-term durability. Similarly, Sengupta et al. (Sengupta et al., 2022a) demonstrated that small differences in tunnel branch diameters led to marked variations in local flow patterns and shear stress oscillations. In our case, a TAWSS threshold of 0.4 Pa was used to assess the risk of intraluminal thrombus, as low WSS is known to promote thrombus formation by facilitating platelet adhesion (Zambrano et al., 2016). Notably, affected regions included the inner wall of the LCCA tunnel and the aortic arch bulge, where recirculating and oscillatory flow patterns were most evident. Similar trends were seen with local elevation of RRT > 15 Pa^{-1} and ECAP > 1.5 Pa^{-1}, where oscillatory shear stress and prolonged particle residence times further indicated a pro-thrombotic environment. Comparable patterns were reported (Da Silva et al., 2024), showing fixation zones and internal branches of a branched modular SG exhibited similarly elevated OSI and RRT values, correlating with low TAWSS and increased thrombotic potential. These findings were supported by the observation of a thrombus at the distal side of the LCCA branch in follow-up, reinforcing abnormal wall shear metrics as indicators of thrombogenic zones and the need for targeted postoperative monitoring.

Forces from blood pressure and WSS are critical for predicting the long-term device structural integrity, device migration, and endoleaks. Peak displacement force reached 14.95 N during mid-diastole – well below the experimentally derived migration threshold of 32 N (Rahmani et al., 2016), suggesting a low likelihood of device migration under physiological loading conditions. However, spatial mapping revealed elevated wall stress concentrated at the proximal and distal landing zones, which likely arises from abrupt changes in material stiffness, suggesting these regions may be susceptible to long-term material fatigue or structural complications. This compliance mismatch can amplify local haemodynamic loads and wall stresses, even though SG implantation effectively isolates the weakened aortic segment from cyclic loading and significantly reduces stresses in vulnerable regions such as the aneurysm sac (Da Silva et al., 2023a). Elevated local wall stress in the landing zones has been associated with adverse events such as dSINE formation (Menichini et al., 2018, Kan et al., 2021, Yoon et al., 2023) or even aortic rupture (Van Bakel et al., 2019). Furthermore, decomposing these forces into components parallel and normal to the vessel wall provides additional predictive insight, with the parallel component linked to the downstream SG migration risk and the normal component to vessel dilation (Duca et al., 2025). Computational simulations incorporating aortic wall distensibility have also demonstrated increased energy loss – an effect severely underestimated by rigid-wall assumptions (Qiao et al., 2021), underscoring the importance of realistic wall mechanics in assessing long-term device performance and aortic remodelling.

Finally, comparisons between rigid-wall CFD and fully coupled FSI simulations revealed that the inclusion of wall compliance attenuated

peak pressures and marginally reduced flow velocities. This dampening effect, absent in rigid-wall CFD models, is crucial for evaluating long-term risks such as wall rupture, graft failure, or adverse remodelling. Consistent findings were reported by da Silva et al. (Da Silva et al., 2023b) who showed that one-way FSI models tend to overestimate haemodynamic parameters during systole, likely due to the lack of fluid energy dissipation. This overestimation was particularly pronounced near local constrictions, such as the aneurysm neck. In the present study, slight deviations between FSI and CFD results at intermediate sections (e.g., P3 and P4) likely reflect the combined effects of local wall motion and complex branching-induced flow patterns, which dampen local flow acceleration and reduce peak velocity magnitudes. These dynamic effects are more accurately captured by the compliant FSI model. In addition to the observed pressure attenuation and velocity reduction, the FSI model predicted a peak wall displacement of approximately 1.16 mm at the mid-descending thoracic aorta (coinciding with the location of high von Mises stress shown in Fig. 4(e)), corresponding to an average lumen area change of 5.9%. Incorporating these insights into our simulations underscores the importance of strongly coupled FSI modelling, especially in complex TEVAR scenarios involving branched geometries and highly compliant aortic segments. Moreover, consistent with the findings of a previous FSI study (Zhu et al., 2022), rigid-wall CFD approaches appear to under-represent areas of low WSS, which may lead to an underestimation of thrombotic risk in susceptible regions.

Despite the results obtained from the FSI simulation, certain limitations remain and should not be overlooked in future work. The use of 4D flow MRI to characterise patient-specific aortic haemodynamics in computational simulation was proposed and validated by Pirola et al. (Pirola et al., 2017), providing a direct means of capturing physiologically realistic velocity distributions for computational modelling. Building on this approach, the generation of synthetic 4D velocity profiles was later introduced by Wang et al. (Wang et al., 2025) to address cases where MRI data are unavailable or of limited quality. In our study, although a carefully tuned synthetic 4D inlet flow profile was adopted, this method inherently depends on population-derived models and may not fully reproduce individual flow asymmetry or pulsatility. Therefore, incorporating patient-specific 4D flow MRI data in future studies would allow more rigorous validation of the simulated haemodynamics and improve confidence in the predictive capability of the FSI framework.

Second, due to compromised image quality, fine geometric details, including the LCCA-LSCA bypass and the implanted SG device, could not be fully resolved. As a result, geometric simplifications were introduced, including a homogenized SG representation that did not explicitly capture the detailed stent-struct configuration or stent-fabric interactions. These simplifications, however, may influence the local flow and stress predictions, and could underestimate fatigue-susceptible regions of the graft under cyclic loading (Sengupta et al., 2022b, Santos et al., 2012). In addition, during the pre-stress initialization, a uniform physiological diastolic pressure was applied to the entire aorta, assuming that the stented and non-stented regions share the same pre-stress state. However, we acknowledge that this may not fully reflect the stress state of the SG device introduced by the implantation procedure.

Furthermore, the material properties and model parameters were adopted from previously validated studies. While these values fall within physiological ranges, their generalization may influence the quantitative accuracy of individual stress and deformation predictions. Therefore, future developments will incorporate a more realistic geometric description of the SG device with improved pre-stress initialization. Techniques such as virtual tensile testing and virtual SG deployment (Kan et al., 2024, Han et al., 2025, Derycke et al., 2019) will be implemented prior to the simulation to enable a better analysis of material sensitivity and more accurately capture the implantation-induced stress, thereby enhancing the overall biomechanical fidelity.

Lastly, as this study focuses on a single case, the generalizability of the findings is limited. The haemodynamic and structural responses observed are likely influenced by the unique anatomical configuration, graft geometry, and branch orientation of this particular case. Variations in aortic curvature, lumen size, or branch locations across patients could lead to markedly different local flow patterns and stress distributions. Future research will incorporate additional cases with diverse anatomical and haemodynamic characteristics to enhance the robustness of the conclusions.

5. Conclusions

This study demonstrated the utility of fully coupled FSI modelling in evaluating the biomechanical and haemodynamic performance of a patient-specific double-branched stent-graft configuration for chronic non-A non-B aortic dissection. The FSI approach, which incorporated vessel wall compliance and physiologically realistic boundary conditions, revealed nuanced flow features and mechanical stresses that were not fully captured by rigid-wall CFD simulations. Importantly, the identification of low WSS, high RRT, and elevated ECAP in regions correlating with observed thrombus formation underscores the clinical relevance of such advanced modelling. The results support the incorporation of FSI into postoperative assessment to better predict potential complications and optimise long-term outcomes in complex endovascular aortic repairs.

CRediT authorship contribution statement

Binghuan Li: Writing – review & editing, Writing – original draft, Visualization, Validation, Software, Methodology, Investigation, Formal analysis, Data curation, Conceptualization. **Yu Zhu:** Writing – review & editing, Writing – original draft, Validation, Supervision, Software, Methodology, Investigation, Formal analysis. **Kaihong Wang:** Writing – review & editing, Validation, Software, Methodology. **Sandro Lepidi:** Writing – review & editing, Supervision, Investigation, Data curation. **Mario D'Oria:** Writing – review & editing, Supervision, Investigation, Data curation, Conceptualization. **Xiao Yun Xu:** Writing – review & editing, Validation, Supervision, Resources, Project administration, Investigation, Funding acquisition, Conceptualization.

Declaration of competing interest

The authors declare that they have no known competing financial interests or personal relationships that could have appeared to influence the work reported in this paper.

Acknowledgements

Binghuan Li is supported by a PhD scholarship from the Department of Chemical Engineering at Imperial College London. Yu Zhu is supported by British Heart Foundation under Grant FS/IPBSRF/23/27098. Binghuan Li would like to thank Giorgos Troulliotis and Xiaoxin Kan for their discussions on solving the Dirichlet-Laplace problem for local fibre direction generation.

Appendix A. Supplementary data

Supplementary data to this article can be found online at https://doi.org/10.1016/j.jbiomech.2025.113126.

References

Burdess, A., D'oria, M., Mani, K., Tegler, G., Lindstrom, D., Mogensen, J., Kolbel, T., Wanhainen, A., 2022. Early experience with a novel dissection-specific stent-graft to prevent distal stent-graft-induced new entry tears after thoracic endovascular repair of chronic Type B aortic dissections. Ann. Vasc. Surg. 81, 36–47.

Chiu, T.L., Tang, A.Y.S., Cheng, S.W.K., Chow, K.W., 2018. Analysis of flow patterns on branched endografts for aortic arch aneurysms. Inf. Med. Unlocked 13, 62–70.

D'oria, M., Neal, D., Budtz-Lilly, J., Cooper, M., De Martino, R., Mani, K., Lepidi, S., Stone, D., Scali, S., 2025. Contemporary trends in practice patterns and clinical

outcomes of thoracic endovascular aortic repair for nontraumatic thoracic aortic disease in the Vascular Quality Initiative. Surgery 181, 109153.
D'oria, M., Wanhainen, A., Kolbel, T., Yoon, W., Mani, K., 2024. Novel insights into thoracic endografts technology for prevention of distal stent-graft induced new entry (dSINE) following endovascular repair of type B aortic dissections: from bench to bedside. Expert Rev. Med. Devices 21, 391–398.
Da Silva, M.L.F., Costa, M.C.B., Goncalves, S.F., Huebner, R., Navarro, T.P., 2024. Numerical analysis of blood flow in a branched modular stent-graft for aneurysms covering all zones of the aortic arch. Biomech. Model. Mechanobiol. 23, 2177–2191.
Da Silva, M.L.F., De Freitas Goncalves, S., Costa, M.C.B., Huebner, R., Navarro, T.P., 2023a. Structural numerical analysis of a branched modular stent-graft for aneurysms encompassing all zones of the aortic arch. J. Mech. Behav. Biomed. Mater. 147, 106135.
Da Silva, M.L.F., Freitas Gonçalves, S.D., Haniel, J., Lucas, T.C., Huebner, R., 2023b. Comparative study between 1-way and 2-way coupled fluid-structure interaction in numerical simulation of aortic arch aneurysms. Anais Da Academia Brasileira De Ciências 95, e20210859.
De Bock, S., Iannaccone, F., De Beule, M., Van Loo, D., Vermassen, F., Verhegghe, B., Segers, P., 2013. Filling the void: a coalescent numerical and experimental technique to determine aortic stent graft mechanics. J. Biomech. 46, 2477–2482.
Derycke, L., Perrin, D., Cochennec, F., Albertini, J.N., Avril, S., 2019. Predictive Numerical Simulations of double Branch Stent-Graft Deployment in an Aortic Arch Aneurysm. Ann. Biomed. Eng. 47, 1051–1062.
Duca, F., Bissacco, D., Crugnola, L., Faitini, C., Domanin, M., Migliavacca, F., Trimarchi, S., Vergara, C., 2025. Computational analysis to assess hemodynamic forces in descending thoracic aortic aneurysms. J. Physiol.
Ferrer, C., Cao, P., Coscarella, C., Ferri, M., Lovato, L., Camparini, S., Di Marzo, L., Investigators, T.R.R., 2019. iTalian RegIstry of doUble inner branch stent graft for arch PatHology (the TRIUmPH Registry). J. Vasc. Surg. 70 (672–682), e1.
Ferrer, C., Tinelli, G., D'oria, M., 2024. Endovascular reconstruction of the aortic arch with new-generation dual-branch and triple-branch endograft: design, applicability, indications, outcomes, and future directions. Expert Rev. Med. Devices 1–9.
Han, X., Zhu, J., Che, Y., Cao, X., Wan, M., Si, X., Wang, W., Shu, C., Luo, M., Zhang, X., 2025. Hemodynamic differences and endoleak risk assessment of different angles of chimney stent graft deployment in chimney technique using integrated structural and fluid dynamics simulation. Biomech. Model. Mechanobiol. 24, 1251–1266.
Iglesias Iglesias, C., Gonzalez Canga, C., Abril Ramiro, F., Alonso Pastor, A., Alvarez Marcos, F., Alonso Perez, M., 2023. An early single-center experience with the Relay double inner-branch arch endograft. J. Thorac. Dis. 15, 6721–6729.
Jorgensen, C.S., Paaske, W.P., 1998. Physical and mechanical properties of ePTFE stretch vascular grafts determined by time-resolved scanning acoustic microscopy. Eur. J. Vasc. Endovasc. Surg. 15, 416–422.
Kan, X., Ma, T., Dong, Z., Xu, X.Y., 2021. Patient-specific Virtual Stent-Graft Deployment for Type B Aortic Dissection: a pilot Study of the Impact of Stent-Graft Length. Front. Physiol. 12, 718140.
Kan, X., Ma, T., Jiang, X., Holzapfel, G.A., Dong, Z., Xu, X.Y., 2024. Towards biomechanics-based pre-procedural planning for thoracic endovascular aortic repair of aortic dissection. Comput. Methods Programs Biomed. 244, 107994.
Kandail, H., Hamady, M., Xu, X.Y., 2014. Patient-specific analysis of displacement forces acting on fenestrated stent grafts for endovascular aneurysm repair. J. Biomech. 47, 3546–3554.
Menichini, C., Pirola, S., Guo, B., Fu, W., Dong, Z., Xu, X.Y., 2018. High Wall stress May Predict the Formation of Stent-Graft-Induced New Entries after Thoracic Endovascular Aortic Repair. J. Endovasc. Ther. 25, 571–577.
Negmadjanov, U., Motta, J.C., Lee, W.A., 2021. Total endovascular aortic arch repair using the Terumo Aortic triple-branch arch endograft. Ann. Vasc. Surg. 77, 351 e7–351 e14.
Pirola, S., Cheng, Z., Jarral, O.A., O'regan, D.P., Pepper, J.R., Athanasiou, T., Xu, X.Y., 2017. On the choice of outlet boundary conditions for patient-specific analysis of aortic flow using computational fluid dynamics. J. Biomech. 60, 15–21.
Qiao, Y., Mao, L., Ding, Y., Fan, J., Zhu, T., Luo, K., 2020. Hemodynamic consequences of TEVAR with in situ double fenestrations of left carotid artery and left subclavian artery. Med. Eng. Phys. 76, 32–39.
Qiao, Y., Mao, L., Ding, Y., Zhu, T., Luo, K., Fan, J., 2021. Fluid-structure interaction: Insights into biomechanical implications of endograft after thoracic endovascular aortic repair. Comput. Biol. Med. 138, 104882.
Rahmani, S., Grewal, I.S., Nabovati, A., Doyle, M.G., Roche-Nagle, G., Tse, L.W., 2016. Increasing angulation decreases measured aortic stent graft pullout forces. J. Vasc. Surg. 63, 493–499.
Ruggeri, A., Magliocco, M., Pane, B., Canepa, M., Seitun, S., Pratesi, G., Menna, C., Morganti, S., Spinella, G., Conti, M., 2025. Patient-specific computational fluid hemodynamics in the ascending aorta before and after thoracic endovascular repair. Comput. Biol. Med. 194, 110493.
Saitta, S., Maga, L., Armour, C., Votta, E., O'regan, D.P., Salmasi, M.Y., Athanasiou, T., Weinsaft, J.W., Xu, X.Y., Pirola, S., Redaelli, A., 2023. Data-driven generation of 4D velocity profiles in the aneurysmal ascending aorta. Comput. Methods Programs Biomed. 233, 107468.
Santos, I.C., Rodrigues, A., Figueiredo, L., Rocha, L.A., Tavares, J.M.R., 2012. Mechanical properties of stent–graft materials. Proceedings of the Institution of Mechanical Engineers, Part l: Journal of Materials: Design and Applications 226, 330–341.
Schussnig, R., Pacheco, D.R.Q., Kaltenbacher, M., Fries, T.-P., 2022. Semi-implicit fluid–structure interaction in biomedical applications. Comput. Methods Appl. Mech. Eng. 400, 115489.
Sengupta, S., Hamady, M., Xu, X.Y., 2022a. Haemodynamic Analysis of Branched Endografts for complex Aortic Arch Repair. Bioengineering (basel) 9.
Sengupta, S., Yuan, X., Maga, L., Pirola, S., Nienaber, C.A., Xu, X.Y., 2023. Aortic haemodynamics and wall stress analysis following arch aneurysm repair using a single-branched endograft. Front. Cardiovasc. Med. 10, 1125110.
Sengupta, S., Zhu, Y., Hamady, M., Xu, X.Y., 2022b. Evaluating the Haemodynamic Performance of Endografts for complex Aortic Arch Repair. Bioengineering (basel) 9.
Subramaniam, D.R., Gutmark, E., Andersen, N., Nielsen, D., Mortensen, K., Gravholt, C., Backeljauw, P., Gutmark-Little, I., 2021. Influence of Material Model and Aortic root Motion in Finite Element Analysis of two Exemplary cases of Proximal Aortic Dissection. J. Biomech. Eng. 143.
Van Bakel, T.M., Arthurs, C.J., Van Herwaarden, J.A., Moll, F.L., Eagle, K.A., Patel, H.J., Trimarchi, S., Figueroa, C.A., 2018. A computational analysis of different endograft designs for Zone 0 aortic arch repair. Eur. J. Cardiothorac. Surg. 54, 389–396.
Van Bakel, T.M.J., Burris, N.S., Patel, H.J., Figueroa, C.A., 2019. Ascending aortic rupture after zone 2 endovascular repair: a multiparametric computational analysis. Eur. J. Cardiothorac. Surg. 56, 618–621.
Wang, K., Armour, C.H., Hanna, L., Gibbs, R., Xu, X.Y., 2025. Generation of personalized synthetic 3-dimensional inlet velocity profiles for computational fluid dynamics simulations of type B aortic dissection. Comput. Biol. Med. 191, 110158.
Ye, X., Zhang, J., Cheng, Z., Lu, F., Wen, Z., Yu, G., Chen, G., Xie, F., Qiao, D., Xing, J., Tan, W., Zhao, D., Ren, M., 2025. Hemodynamic modeling of aortic arch aneurysm treatment using the Castor branched stent graft: a virtual coil embolization simulation framework. Front. Physiol. 16, 1629346.
Yoon, W.J., Mani, K., Wanhainen, A., 2023. Computational Fluid Dynamics Analysis of a New Dissection specific Stent Graft with the Aim to prevent Distal Stent Graft Induced New Entry (dSINE). Eur. J. Vasc. Endovasc. Surg. 66, 146–147.
Zambrano, B.A., Gharahi, H., Lim, C., Jaberi, F.A., Choi, J., Lee, W., Baek, S., 2016. Association of Intraluminal Thrombus, Hemodynamic Forces, and Abdominal Aortic Aneurysm expansion using Longitudinal CT Images. Ann. Biomed. Eng. 44, 1502–1514.
Zhang, X., Xiong, J., Ma, W., Xue, L., Xu, Z., Zhang, H., Wang, Y., Chen, D., Guo, W., 2024. Evaluation of embedded modular branched stent graft in treating aortic arch aneurysm using imaging-based computational flow analysis. Med. Novel Technol. Devices 21, 100285.
Zhu, Y., Armour, C., Li, B., Pirola, S., Salmasi, Y., Athanasiou, T., O'regan, D.P., Xu, X.Y., 2025a. A combined 4D flow MR imaging and fluid-structure interaction analysis of ascending thoracic aortic aneurysms. Biomech. Model. Mechanobiol. 24, 829–844.
Zhu, Y., Mirsadraee, S., Rosendahl, U., Pepper, J., Xu, X.Y., 2022. Fluid-Structure Interaction Simulations of Repaired Type A Aortic Dissection: a Comprehensive Comparison with rigid Wall Models. Front. Physiol. 13, 913457.
Zhu, Y., Pirola, S., Salmasi, M.Y., Sasidharan, S., Fisichella, S.M., O'regan, D.P., Moore Jr., J.E., Athanasiou, T., Xu, X.Y., 2025b. The influence of material properties and wall thickness on predicted wall stress in ascending aortic aneurysms: a finite element study. Cardiovasc. Eng. Technol. 16, 52–65.
Zhu, Y., Zhan, W., Hamady, M., Xu, X.Y., 2019. A pilot study of aortic hemodynamics before and after thoracic endovascular repair with a double-branched endograft. Med. Novel Technol. Devices 4, 100027.